IRSTI 29.19.22 https://doi.org/10.26577/phst20251223

Kubelka-Munk function, Urbach energy and Kramer–Kronig method in porous silicon

F. Alfeel

Department of Medical Physics, University of Al-Farahidi, Baghdad, Iraq
e-mail: faten.hussein@uoalfarahidi.edu.iq
(Received June 7, 2025; received in revised form November 30, 2025; accepted December 7, 2025)

Porous silicon (PS) samples were fabricated using electrochemical etching and characterized by atomic force microscopy, which showed that the surface roughness increases with porosity. The optical properties and the influence of porosity were investigated through specular and diffuse reflectance, transmission, and absorption measurements. Analysis of the diffuse reflectance spectra using the Kubelka–Munk function revealed that the optical band gap widens as porosity increases, indicating modifications in the electronic structure due to pore formation. The Urbach energy, determined from the absorption edge, also increases with porosity as a result of the higher density of unsaturated surface bonds. The dielectric constant, calculated via the Kramers–Kronig method, shows an increase in both its real and imaginary components with higher porosity, confirming the enhanced energy-storage capability of PS. Thermal energy-loss values likewise rise with pore content. Overall, the results demonstrate that increasing porosity significantly alters the optical and dielectric properties of porous silicon, supporting its potential applications in optoelectronic and energy-storage devices.

Keywords: Porous silicon, Kubelka–Munk function, Urbach energy, dielectric constant, Kramers–Kronig method, refractive index.
PACS number(s): 78.20.Ci, 78.40.-q -, 02.30.-f, 81.07.-b -, 78.30.-j.

1. Introduction

Porous silicon (PS) has attracted substantial interest in recent years owing to its remarkable physicochemical and optoelectronic characteristics, including visible luminescence, tunable refractive index, adjustable energy band gap, and low optical absorption in the visible range [1]. Its high internal surface area, variable surface chemistry, and morphology-dependent porosity, along with its strong light–matter interaction [2] and controllable thermal properties [3], further enhance its technological relevance. These attributes, combined with the relative ease of fabricating well-defined layered structures, have enabled the development of a wide range of PS-based optoelectronic devices, such as light-emitting components, wavelength-selective photodetectors, optical sensors, and Bragg reflectors [4]. Carbon-coated PS has also been incorporated into palladium-based catalysts for safe hydrogen storage, demonstrating improved efficiency and humidity tolerance compared to existing commercial alternatives [5]. Moreover, PS has been explored as a means of enhancing solar-cell efficiency [6,7].

Diffuse reflectance spectra have been widely used to estimate the optical band gap by fitting it to multiple absorption mechanisms for different materials, while Kramers–Kroning transformation has enabled the extraction of dielectric constants from the same measurements [8]. The Urbach tail, which characterizes the degree of disorder near the band edge, has been evaluated via the generalized Tauc–Lorentz method [9]. PS can exhibit extremely high optical absorption, with reported values approaching 99.75% absorption at selected frequencies; this absorption can be dynamically tuned by varying external parameters such as pump-beam fluence [10]. Integration of PS with materials like Vanadium dioxide (VO_2) further enhances its tunability, enabling phenomena such as electromagnetically induced transparency (EIT) and narrow-band absorption that are controllable through temperature or optical pumping [11]. Such hybrid

systems are compatible with modern semiconductor processing techniques, expanding their potential for advanced optoelectronic applications [12].

Although several studies have investigated the physical properties of PS and the influence of individual fabrication [13], the literature lacks a systematic, comparative analysis of how different manufacturing conditions simultaneously affect key optical descriptors–namely, the band gap derived from the Kubelka–Munk function, the degree of band-edge disorder assessed through the Urbach energy, and the dielectric response obtained from the Kramers–Kronig method. Similarly, a coherent examination of surface roughness, its dependence on porosity, and its relationship to fabrication parameters across two groups of samples within a single study has not yet been reported.

This work provides a comprehensive analysis that systematically correlates the optical properties of porous silicon with key fabrication parameters, including current density and HF concentration, as well as surface roughness and porosity. By preparing samples under controlled variations of these parameters, the study establishes quantitative relationships and offers deeper insight into how different manufacturing conditions influence the resulting optical behavior. The findings presented here serve as a valuable reference for future researchers and designers developing hybrid optoelectronic systems, providing an essential materials database for advanced device engineering.

2. Theoretical basis for optical and structural parameter calculations

2.1. Porosity and film thickness

The influence of the HF concentration and current density on the porosity was studied by performing anodic etching under various combinations of these parameters and characterizing the resulting PS samples. The porosity *P* of PS is defined as the fraction of void volume within the porous layer and can be easily determined via using standard gravimetric measurements [14]

$$P(\%) = \frac{m_1 - m_2}{m_1 - m_3} \quad (1)$$

where m_1 is mass of the pristine silicon wafer prior anodization, m_2 is the mass immediately after anodization, m_3 is the mass after complete dissolution of the porous layers in a molar NaOH aqueous solution. The selective removal of the PS layer is achieved by immersing the sample for several minutes in a 3% NaOH solution, which dissolves the porous silicon without affecting the underlying crystalline substrate.

The thickness *L* of the porous layer was also determined gravimetrically using:

$$L = \frac{m_1 - m_3}{\rho S} \quad (2)$$

where ρ is the density of bulk silicon and S is the etched surface area [14].

Additionally, the film thickness *L* was calculated from the reflectance spectrum using Eq. (3), based on the separation between two adjacent interference peaks with refractive indices of n_1 and n_2 and corresponding wavelengths of λ_1 and λ_2 [13]:

$$L = \frac{\lambda_1 \lambda_2}{2(\lambda_1 n_2 - \lambda_2 n_1)} \quad (3)$$

2.2. Diffuse reflectance spectroscopy (DR) and the Kubelka-Munk function

Diffuse refraction spectra (DRS) were converted into equivalent absorption spectra using the Kubelka–Munk formalism, which is widely employed for determining the optical band gap of porous and powdered materials [15-18].

$$F(R) = \frac{K}{S} = \frac{(1-R)^2}{2R} \quad (4)$$

where *F(R)* is the Kubelka–Munk function, *R* is the diffuse reflectance of the film as a function of the wavelength, S and K denote the scattering and absorption Kubelka–Munk coefficients, respectively.

The energy band gap was then extracted by plotting $(F(R) * hf)^n$ as a function of photon energy (hf), where the exponent n takes the value of 2 for direct allowed transitions and 1/2 for indirect allowed transitions [16]. The linear portion of the resulting Tauc plot was extrapolated to the energy axis to obtain the corresponding band gap.

2.3. Urbach energy tail E_u

The Urbach energy is an important parameter that characterizes the density of localized defect states within the band-gap region. These defect states–arising from structural disorder, lattice imperfections, and incomplete surface passivation–give rise to an exponential absorption tail in the sub-band-gap

region of the optical spectrum, known as the Urbach tail. This tail reflects absorption contributions from both the crystalline lattice and dopant-related states. The magnitude of this tail, quantified as the Urbach energy, provides insight into the degree of disorder present in the material. The Urbach energy can be extracted from absorption spectra using the empirical relation [9,17,19]:

$$\alpha = \alpha_o Exp(\frac{E}{E_u}) \quad (5)$$

where E_u is the Urbach energy, α is the absorption coefficient and α_o is a material-dependent constant. The incident photon energy is given by $E = hf$, where h is a Plank's constant and f is photon frequency.

The absorption coefficient can also be calculated from equation [17]:

$$\alpha = \frac{A}{L} \quad (6)$$

where L is the thickness of the film and A is the absorption.

According to the Beer–Lambert's law [20]:

$$A = -Ln(T) \quad (7)$$

Therefore, equation (6) can be written as [15]:

$$\alpha = -\frac{\ln(T)}{L} \quad (8)$$

The refractive index n and extinction coefficient k can be calculated as follows [19-21]:

$$n = \frac{1-R_{spec}}{1+R_{spec}-2\sqrt{R_{spec}}\,cos\theta} \quad (9)$$

$$k = \frac{2\sqrt{R_{spec}}\,sin\theta}{1+R_{spec}-2\sqrt{R_{spec}}\,cos\theta} \quad (10)$$

where R_{spec} represents the specular reflectance of the PS.

The dielectric constant describes the ability of a material to store electrical energy when subjected to an external electric field. It is expressed as a complex quantity comprising two components: a real part and an imaginary part. The real component represents the amount of energy stored elastically within the material; thus, higher values of the real dielectric constant indicate greater energy-storage capability. In contrast, the imaginary component corresponds to dielectric losses, reflecting the amount of energy dissipated as heat. Consequently, an increase in the imaginary dielectric constant signifies greater thermal energy loss under an applied electric field [21,22].

The complex dielectric function can be calculated using the following relations [20]:

$$\tilde{\varepsilon} = \varepsilon_r + i\varepsilon_i$$

$$\varepsilon_r = n^2 - k^2 \quad (11)$$

$$\varepsilon_i = 2nk \quad (12)$$

where $\tilde{\varepsilon}$ is a complex dielectric constant, ε_r and ε_i are its real and imaginary components, and n and k are the refractive index and extinction coefficient, respectively.

3. Materials and methods

Two groups of n-type crystalline silicon (c-Si) wafers with a (100) orientation were electrochemically etched in hydrofluoric acid (HF) solutions of varying concentrations. In the first group samples were etched in 20% HF (by volume) at different current densities of 30, 40, and 50 mA/cm² for 5 minutes. The second group was fabricated using HF solutions of 25%, 30%, and 35% (by volume) at a fixed current density of 20 mA/cm² for 10 minutes. After anodization, all the samples of PS were gently removed, rinsed in deionized water, and dried. The presence of PS was initially confirmed through its characteristic photoluminescence under UV illumination [1–3, 23]. The full set of fabrication parameters is summarized in Table 1.

Atomic force microscopy (AFM) was employed to accurately assess both porosity and surface roughness. Optical scattering measurements were conducted using an integrating sphere attached to a spectrophotometer operating over the 350–2500 nm wavelength range.

A central objective of this study is to examine how the porosity of silicon influences its optical properties–most notably the energy band gap and dielectric constant–and to establish quantitative relationships between structural parameters and optical responses.

Table 1 – Fabrication parameters of the PS samples.

PS n-type Samples	HF concentration (%)	Anodization time(min)	Current density (mA/cm^2)	Porosity%
S1	20	5	30	30.8 ± 0.05
S2	20	5	40	32.28 ± 0.05
S3	20	5	50	33 ± 0.05
S4	25	10	20	17 ± 0.05
S5	30	10	20	14 ± 0.05
S6	35	10	20	9 ± 0.05

4. Results and discussion

The porosity (p%) increases with increasing current density, as shown in Fig.1a. At low current densities, the number of charge carriers is limited, resulting in minimal silicon dissolution along the current path and, consequently, low porosity. At higher current densities, the increased availability of charge carriers enhances dissolution, leading to higher porosity [24].

Similarly, the porosity (p%) increases as the HF concentration decreases, as shown in Fig.1b. Lower HF concentrations promote greater silicon dissolution, effectively increasing the critical current density at the oxide–silicon interface. As the HF concentration increases, the pore structure becomes finer and the pore walls thicken, resulting in a reduction in overall porosity [25].

Atomic force microscopy (AFM) was employed to examine the surface morphology of the PS samples and to quantify their surface roughness. Fig. 2 presents 2D AFM images of the investigated samples. These measurements were used to establish the relationship between surface roughness and the fabrication conditions applied during sample preparation.

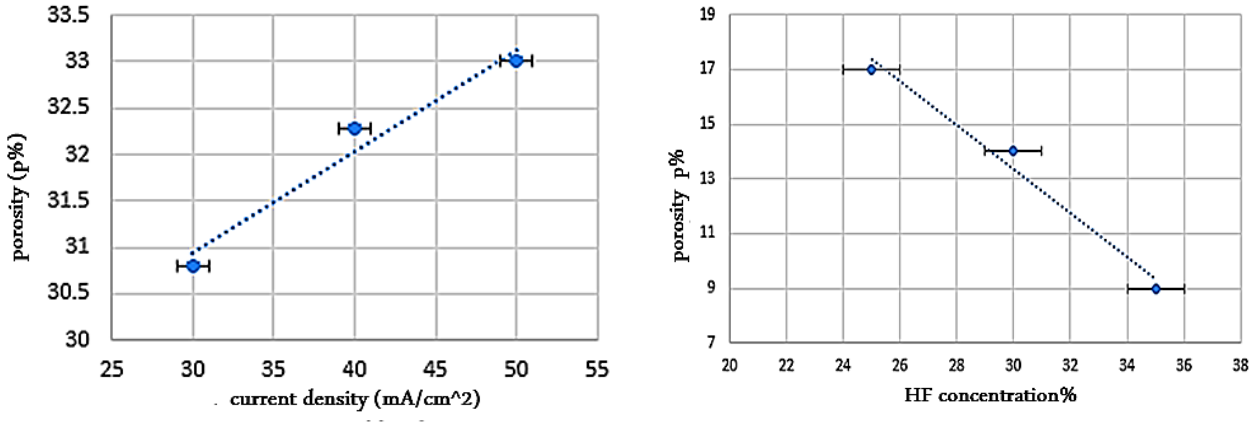

a) b)

Figure 1 – (a) Porosity (p%) of the PS layers as a function of current density for samples etched at 20% HF.
(b) Porosity (p%) of the PS layers as a function of HF concentration for samples etched at a fixed time and current density.

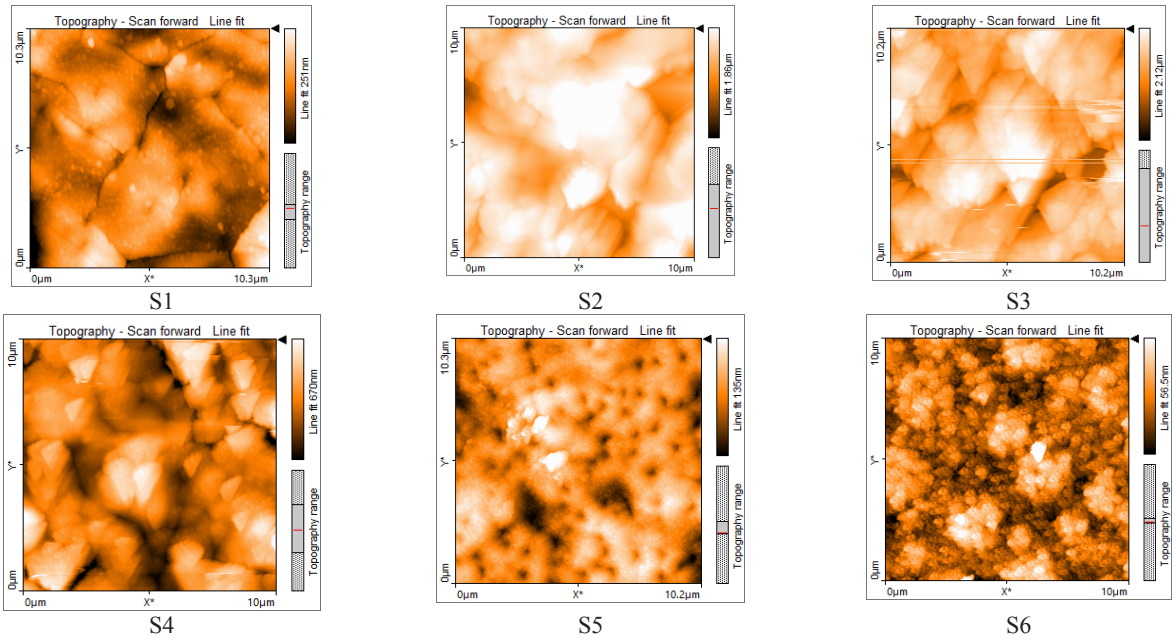

Figure 2 – 2D AFM images (10 × 10 μm^2) of PS.

The introduction of pores into crystalline silicon inherently increases surface roughness, as greater porosity corresponds to a larger number of pores that disrupt the initially smooth surface. As shown in Fig.3, the surface roughness increases systematically with increasing porosity, consistent with the accompanying increase in effective surface area.

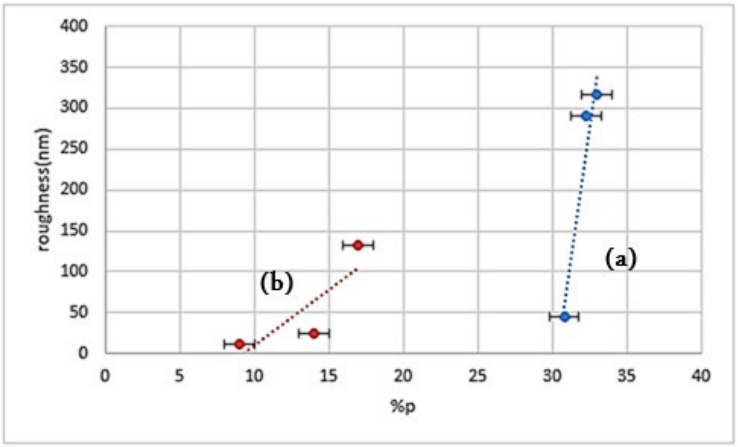

Figure 3 – Surface roughness vs porosity of PS samples:
(a) PS samples prepared at different current densities;
(b) PS samples prepared at different HF concentrations.

The optical properties of the PS samples were studied using a UV–Vis–NIR spectrophotometer to record diffuse reflectance (DR) spectra (Fig. 4). Due to the roughened surface of PS, incident light is primarily scattered rather than specularly reflected. The nanoscale features within the porous layer give rise to distinct light–matter interactions, including interference effects in both the ultraviolet and visible regions of the spectrum, whereas the infrared region remains relatively flat. When light interacts with pores whose dimensions are comparable to the incident wavelength, resonant scattering occurs, producing

constructive or destructive interference with the scattered waves. This process strongly influences the transmittance, absorption, and reflectance properties of the material. Small pores preferentially scatter shorter wavelengths, while larger pores are more effective at scattering longer wavelengths. Furthermore, the presence of pores facilitates partial confinement of light within the silicon matrix, thereby modifying the effective optical path and altering the measured reflectance and absorption values [26].

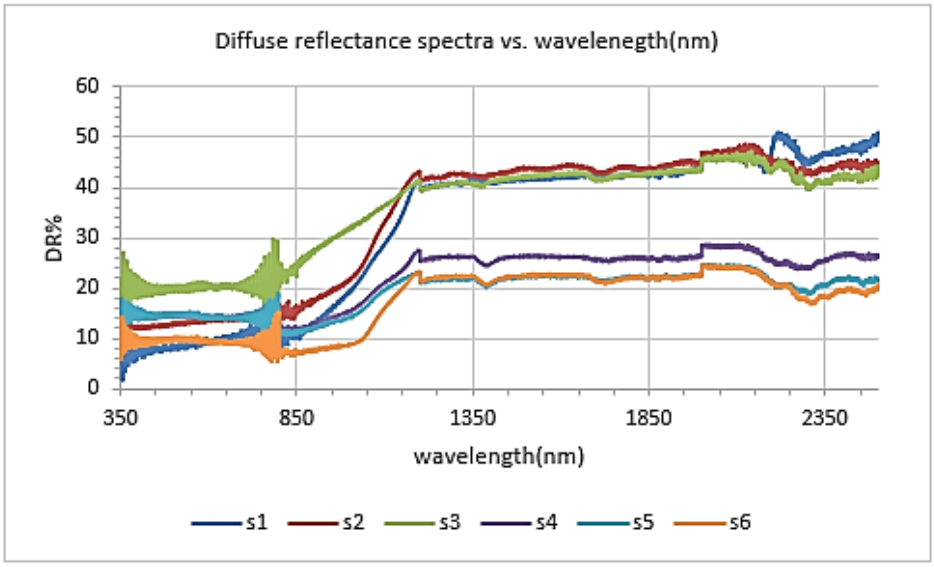

Figure 4 – DR spectra (expressed in %) of the PS samples recorded across the 350–2500 nm wavelength range.

Fig. 5 shows the spectra of the transmittance (T) as a function of the wavelength. The transmittance increases as the porosity increases because more pores make silicon more transparent.

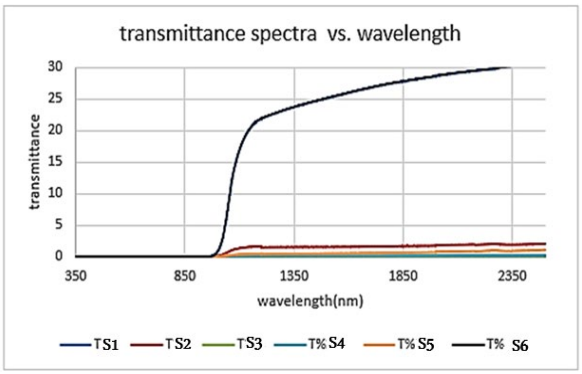

Figure 5 – Transmittance spectra of the PS samples measured over the wavelength range of 350–2500 nm.

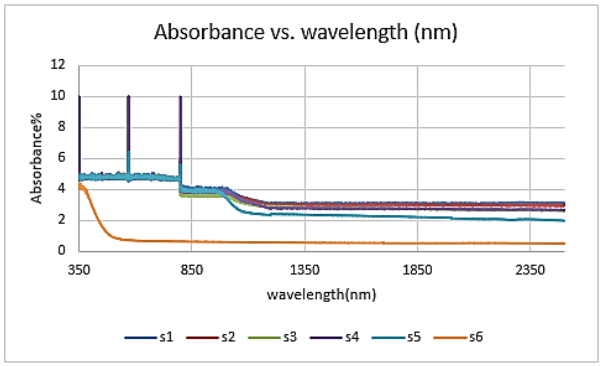

Figure 6 – Absorbance spectra of the PS samples recorded across the 350–2500 nm wavelength range.

The transmittance (T) spectra of the PS samples were used to calculate the absorption coefficient using Eq. (8). As shown in Fig. 6, the absorbance increases with increasing porosity. This behavior arises because pores partially trap incoming light: a portion of the light is transmitted through the porous

network, while the remainder is absorbed by the silicon walls surrounding the pores.

Using Eq. (9), the refractive index of the PS samples at a fixed wavelength of 808 nm was determined. As illustrated in Fig. 7, the refractive index increases with increasing porosity. This trend occurs because light propagates more rapidly through air-filled pores than through dense silicon; thus, a higher pore fraction results in an overall effective refractive index governed by an effective medium approximation. The refractive index of porous silicon therefore differs substantially from that of bulk crystalline silicon [1].

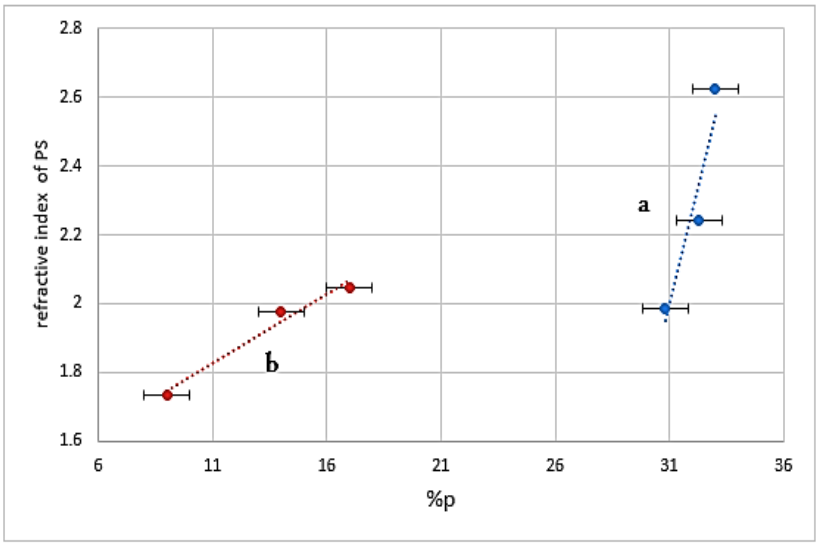

Figure 7 – Refractive index of PS samples at 808 nm as a function of porosity.
(a) PS samples prepared at different current densities;
(b) PS samples prepared at different HF concentration.

The energy band gap E_g was calculated using the Kubelka–Munk function, by plotting $(F(R) * hf)^n$ versus (hf) for n =2, corresponding to a direct allowed transition (Figure 8). The energy gap value was extracted from the intercept of the linear portion of the plot with the energy axis. The E_g values for PS samples are larger than that of bulk silicon, consistent with the presence of nanoscale silicon structures. As porosity increases, the remaining silicon frameworks become thinner and approach characteristic dimensions where quantum confinement becomes significant, leading to a widening of the energy band gap [26].

Fig. 9 shows the dependence of the optical band gap on porosity. For samples prepared at different current densities, the band gap increases from 1.87 eV to 3.26 eV as the porosity increases from 30.8% to 33%. Similarly, for samples fabricated at different HF concentrations, the band gap increases from 1.76 eV to 3.30 eV as porosity rises from 9% to 17%. When pores form within silicon at dimensions comparable to the de Broglie wavelength of charge carriers (electrons and holes), quantum confinement effects emerge. This confinement restricts carrier motion, discretizes the energy levels, and prevents the formation of a continuous energy band structure, thereby widening the band gap. The formation of localized energy states near the porous silicon surface also modifies the electronic properties and influences the carrier concentration [24].

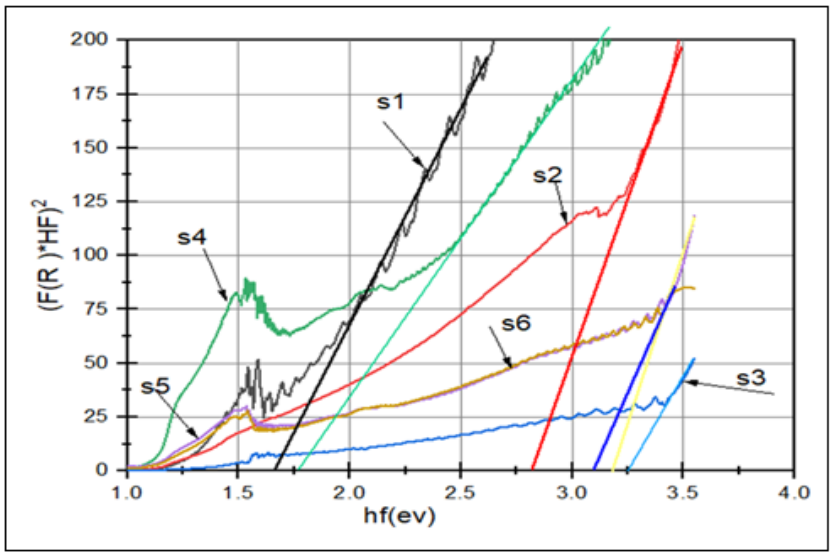

Figure 8 – Plots of $(F(R) * hf)^n$ versus (hf), used to determine the optical band gap of PS samples based on the Kubelka–Munk function.

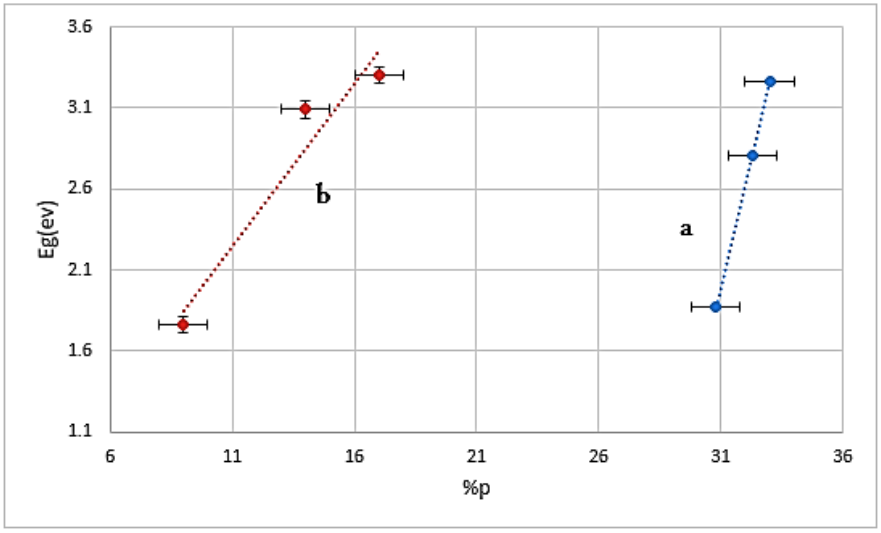

Figure 9 – Optical band gap as a function of porosity (p%) for the PS samples.
(a) Samples prepared at different current densities. (b) Samples prepared at different HF concentrations.

The absorption coefficient was calculated from the transmittance spectrum using Eq. (8), and the Urbach energy (Eu) was then determined using Eq. (5) by plotting $\ln(\alpha)$ versus hf. The inverse of the slope of linear region of this plot (illustrated for sample S1 in Fig. 10) yields the Urbach energy for each sample.

As shown in Fig. 11, the Urbach energy increases from 0.311 eV to 0.93 eV as porosity rises from 30.8% to 33% for samples prepared at different current densities. For samples prepared at varying HF concentrations, Eu increases from 0.1136 eV to 0.6696 eV as porosity increases from 9% to 17%. All values were obtained using identical procedures.

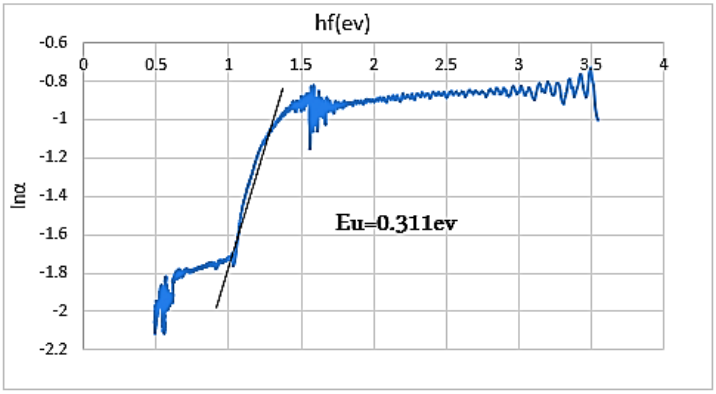

Figure 10 – Plot of ln(α) versus hf for determining the Urbach energy of sample S1.

The Urbach energy, often referred to as correlation energy, represents the energy required to break chemical bonds at the material surface and is closely associated with structural disorder and the presence of dangling or incomplete bonds [27]. As porosity increases, the number of such defect states grows, resulting in a corresponding increase in the Urbach energy.

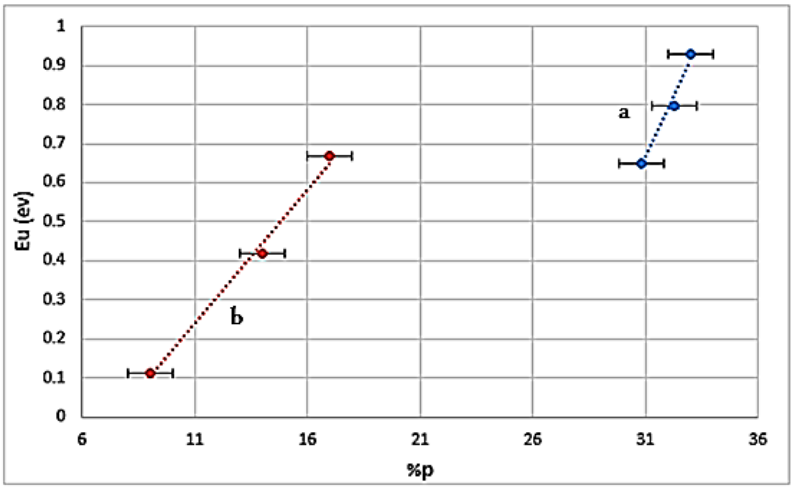

Figure 11 – Urbach energy as a function of porosity (P%P%) for the PS samples.
(a) Samples prepared at different current densities.
(b) Samples prepared at different HF concentrations.

The real part of the dielectric constant was calculated using Eq. (11), while the imaginary part was obtained using Eq. (12). At a wavelength of 808 nm, both components of the dielectric constant for the PS samples are shown in Figures 12 and 13. The results demonstrate that both the real and imaginary parts of the dielectric constant increase with increasing porosity. The incorporation of pores enhances the overall polarity of the material, thereby increasing the real dielectric constant. At the same time, the presence of pores promotes stronger scattering and confinement of electromagnetic waves, which leads to higher dielectric losses and thus a larger imaginary component. As shown previously in Fig. 11, higher porosity also corresponds to increased Urbach energy, indicating a greater density of defect states. These surface states may serve as active sites for interactions with

particles such as protons or secondary ions, making porous silicon a promising candidate for catalytic and biosensing applications [28].

The increase in the real part of the dielectric constant with porosity is particularly relevant for applications requiring materials with tunable dielectric behavior. High-dielectric porous layers can function as active components in ferroelectric capacitors, ferroelectric field-effect transistors (FeFETs), and ferroelectric tunneling junctions (FTJs), or as low-index interlayers in optical and electronic device architectures [29]. Conversely, a higher imaginary dielectric constant reflects increased energy dissipation, which is undesirable in photonic circuits where losses must be minimized, but advantageous in photothermal processing, where efficient heat generation is required.

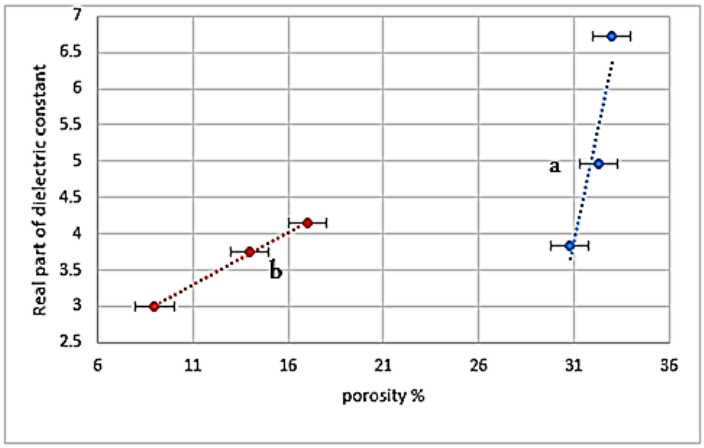

Figure 12 – Real part of the dielectric constant (ε_r) of the PS samples at 808 nm as a function of porosity. (a) Samples prepared at different current densities. (b) Samples prepared at different HF concentrations.

Porosity also directly influences the specific surface area of PS; as the surface area increases, the material exhibits enhanced responsiveness under an applied electric field [26]. Furthermore, the emergence of additional defect levels modifies the polarization behavior of the material [30]. Previous results have shown that changes in the energy band gap due to porosity alter the electronic structure and optical transitions within the material [31], which in turn impacts the dielectric response. As silicon transitions from a bulk semiconductor to a porous structure with a wider band gap, its absorption and transmission characteristics change accordingly, leading to corresponding variations in the dielectric constant [32].

Table 2 summarizes the results obtained in this study. Samples S1, S2, and S3 were fabricated by varying the current density while keeping the HF concentration and etching time constant. Their porosity increased from 30.8% to 33% with increasing current density. Correspondingly, the optical band gap expanded from 1.87 eV to 3.26 eV, while the Urbach energy increased from 0.649 eV to 0.930 eV. Surface roughness showed a pronounced rise, from 44.3 nm to 316.0 nm. The real part of the dielectric constant increased from 3.838 to 6.733, and the imaginary part increased from 0.745 to 2.47.

Samples S4, S5, and S6–prepared by varying the HF concentration while maintaining constant current density and etching time–showed the expected trend that higher HF concentrations yield lower porosity. When the samples are ranked by increasing porosity, they similarly show an increase in band gap from 1.76 eV to 3.30 eV and a rise in Urbach energy from 0.114 eV to 0.669 eV. Surface roughness increased from 11.1 nm to 131.6 nm. The real part of the dielectric constant increased from 2.99 to 4.148, while the imaginary part increased from 0.427 to 0.836.

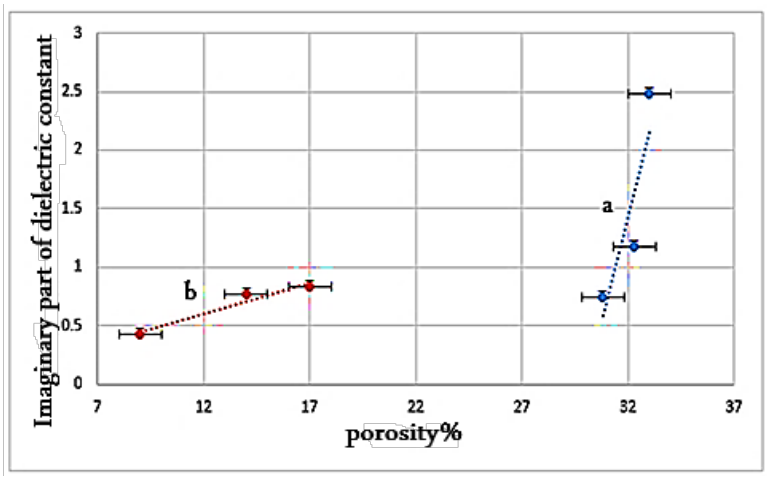

Figure 13 – Imaginary part of the dielectric constant (ε_i) of the PS samples at 808 nm as a function of porosity. (a) Samples prepared at different current densities. (b) Samples prepared at different HF concentrations.

Table 2 – Summary of optical and structural properties of PS samples.

Sample	S1	S2	S3	S4	S5	S6
Porosity% ∓0.05	30.8	32.28	33	17	14	9
Refractive index nps ∓0.001	1.97	2.24	2.63	2.05	1.98	1.74
E_g (ev) ∓0.0002	1.87	2.81	3.26	3.3	3.09	1.76
Roughness (nm) (∓0.005)	44.30	290.06	316.03	131.57	24.51	11.14
E_u (ev) (0.001)	0.649	0.795	0.930	0.669	0.417	0.114
$\varepsilon_i \mp 0.001$	0.745	1.178	2.477	0.836	0.765	0.427
$\varepsilon_r \mp 0.001$	3.838	4.959	6.733	4.148	3.757	2.991
Film thickness(nm)∓5nm	13620	14274	14592	948.63	781.22	502.22

5. Conclusion

This study demonstrates clear correlations between fabrication parameters and the fundamental optical and dielectric properties of porous silicon. By varying current density and HF concentration across two groups of samples, we observed systematic increases in porosity, which in turn led to higher optical band gaps, larger Urbach energies, increased surface roughness, and enhanced real and imaginary components of the dielectric constant. These trends reflect the growing density of defect states and the stronger light–matter interactions introduced by the porous structure.

The results highlight the strong dependence of PS properties on its fabrication conditions and underscore the importance of porosity as a key tuning parameter. These findings provide useful guidelines for the design of porous silicon components in optoelectronic devices, sensors, and hybrid materials. Moreover, the work opens pathways for further functionalization, including filling pores with tailored materials to achieve application-specific performance. Overall, this study links fundamental materials characterization with practical engineering considerations for future PS-based technologies.

Acknowledgments: I'm very grateful to Head of the Physics Department at the Faculty of Science at Damascus University, prof. Iyad Madwar, for helping me preparing samples, conduct measurements, and allow me to use the university's scientific research laboratories.

References

1. Alfeel F., Awad F., Qamar F. Tunable optical properties of porous silicon of p-type porous silicon // Damascus University Journal for the Basic Sciences. – 2014. – Vol. 30, No. 2. – Pp. 41–51.

2. Alfeel F., Awad F., Qamar F. Change of diffused and scattered light with surface roughness of p-type porous silicon // International Journal of Nano Dimensions. – 2014. – Vol. 5, No. 4. – Pp. 415–419. https://doi.org/10.7508/ijnd.2014.04.014

3. Alfeel F., Awad F., Qamar F. Changes of thermal conductivity, optical conductivity and electric conductivity of porous silicon with porosity // Journal of New Technology in Materials. – 2013. – Vol. 3, No. 1. – Pp. 56–60. https://doi.org/10.12816/0010281

4. Torres-Costa V., Martín-Palma R.J. Application of nanostructured porous silicon in the field of optics: A review // Journal of Materials Science. – 2010. – Vol. 45, No. 11. – Pp. 2823–2838. https://doi.org/10.1007/s10853-010-4251-8

5. Baktygerey S.Z. et al. Palladium catalysts supported on carbonized porous silicon for H_2/O_2 recombination // Physical Sciences and Technology. – 2023. – Vol. 10, No. 2. – Pp.40-47. https://doi.org/10.26577/phst.2023.v10.i2.05

6. Salman K.A., Hassan Z., Omar K. Effect of silicon porosity on solar cell efficiency // International Journal of Electrochemical Science. – 2012. – Vol. 7, No. 1. – Pp. 376–386.

7. Mussabek G., Mirgorodskij I., Kharin A., Taurbayev T., Timoshenko V. Formation and optical properties of nanocomposite based on silicon nanocrystals in polymer matrix for solar cell coating // J. Nanoelectron Optoelectron. -2015, -Vol. 9, --No. 6, -Pp. 738-740. https://doi.org/10.1166/jno.2014.1670

8. Nowak M., Kauch B., Szperlich P. Determination of energy band gap of nanocrystalline SbSI using diffuse reflectance spectroscopy // Review of Scientific Instruments. – 2009. – Vol. 80, No. 4. – Art. 046107. https://doi.org/10.1063/1.3103603

9. Riungu G.G., Mugo S.W., Ngaruiya J.M., John G.M., Mugambi N. Optical band energy, Urbach energy and associated band tails of nanocrystalline TiO_2 films at different annealing rates // American Journal of Nanosciences. – 2021. – Vol. 7, No. 1. – Art. 28. https://doi.org/10.11648/j.ajn.20210701.15

10. Wang Y., Yue L., Cui Z., Zhang X., Zhu Y., Zhang K. Optically tunable single narrow band all-dielectric terahertz metamaterials absorber // AIP Advances. – 2020. – Vol. 10, No. 4. – Art. 045039. https://doi.org/10.1063/5.0003817

11. Zhang X., Wang G., Liu J., Zuo S., Li M., Yang S., Jia Y., Gao Y. Switchable and tunable terahertz metamaterial based on vanadium dioxide and photosensitive silicon // Nanomaterials. – 2023. – Vol. 13. – Art. 2144. https://doi.org/10.20944/preprints202306.1936.v1

12. Hao D., Zhang Y., et al. Silicon bowtie structure based adjustable nonrigid all-nonmetal metamaterial terahertz filter // Optics Letters. – 2022. – Vol. 47, No. 23. – Pp. 6101–6104. https://doi.org/10.1364/ol.471704

13. Manakov S.M., Sagidolda Ye. Investigation of the physical properties of nanoscale porous silicon films // Physical Sciences and Technology. – 2015. – Vol. 2, No. 1. – Pp. 4–8. https://doi.org/10.26577/2409-6121-2015-2-1-4-8

14. Alfeel F.M. Optical properties of ZnO film on porous silicon p-type substrate // Damascus University Journal for the Basic Sciences. – 2025. – Vol. 41, No. 1. – Pp. 101–115.

15. Chryssou K., Stassinopoulou M., Lampi E. A study of the optical bandgap energy and Urbach energy tail of two white A4 copy paper samples // Annals of Chemical Science Research. – 2021. – Vol. 3, No. 1. Art. 000551. https://doi.org/10.31031/ACSR.2021.03.000551

16. Venkatesan R., Mayandi J., Pearce J.M., Venkatachalapathy V. Influence of metal assisted chemical etching time period on mesoporous structure in upgraded metallurgical grade silicon for solar cell application // Journal of Materials Science: Materials in Electronics. – 2019. – Vol. 30, No. 9. – Pp. 8676–8685. https://doi.org/10.1007/s10854-019-01191-6

17. Mussabek G.K., Yermukhamed D., Suleimenova Z. A., Assilbayeva R. B., Sivakov, V. A., Zavestovskaya. I. N., V.Yu. Timoshenko. Reflectance modification in nanostructured silicon layers with gradient porosity // Bulletin of the Lebedev Physics Institute. – 2019, -Vol. 46, – No.10, -Pp. 314-318. https://doi.org/10.3103/S106833561910004X

18. Dejam, Sabbaghzadeh J., Ghaderi A., Solaymani S., Matos R.S., Ţălu Ş., Henrique D., Sari A.H., Kiani M., Amir A., Doudaran M.A. Advanced nano-texture, optical bandgap, and Urbach energy analysis of NiO/Si heterojunctions // Scientific Reports. – 2023. – Vol. 13, No. 1. – Art. 3766. https://doi.org/10.1038/s41598-023-33713-y

19. Norouzzadeh P., Mabhouti Kh., Golzan M.M., Naderali R. Investigation of structural, morphological and optical characteristics of Mn-substituted Al-doped ZnO nanoparticles: A Urbach energy and Kramers–Kronig study // Optik. – 2020. – Vol. 204. – Art. 164227. https://doi.org/10.1016/j.ijleo.2020.164227

20. BYJU'S. Derivation of Beer–Lambert law [Electronic resource]. – 2018. – Available at: https://byjus.com/physics/derivation-of-beer-lambert-law (available on December 15, 2025).

21. Nazari N., Golzan M.M., Mabhouti Kh. Study of Urbach energy and Kramers–Kronig on Mn- and Zn-doped $NiFe_2O_4$ ferrite nanopowder for the determination of structural and optical characteristics // Scientific Reports. – 2024. – Vol. 14, No. 1. – Art. 6407. https://doi.org/10.1038/s41598-024-57045-7

22. Singh K.P., Bhattacharjee S. Optical parameters of atomically heterogeneous systems created by plasma-based low energy ion beams // Frontiers in Physics. – 2021. – Vol. 9. Art. 671137. https://doi.org/10.3389/fphy.2021.671137

23. Zhanabaev Z., Ibraimov M., Sagidolda Y. Nonlinear electrical properties of nanostructured porous silicon films // Physical Sciences and Technology. – 2014. – Vol. 1, No. 1. – Pp. 69–73. https://doi.org/10.26577/phst-2014-1-17

24. Solanki C.S., Bilyalov R., Poortmans J., et al. Self-standing porous silicon films by one-step anodizing // Journal of the Electrochemical Society. – 2004. – Vol. 151, No. 5. – Pp. C307–C313. https://doi.org/10.1149/1.1688797

25. Burham N., Hamzah A.A., Majlis B.Y. Effect of hydrofluoric acid concentration on pore size diameter of silicon membrane // Bio-Medical Materials and Engineering. – 2014. – Vol. 24, No. 6. – Pp. 2203–2209. https://doi.org/10.3233/BME-141032

26. Sze S.M., Ng K.K. Physics of semiconductor devices. – Hoboken: Wiley, 2006, 815 p. https://doi.org/10.1002/0470068329

27. Sivaprakash P., Venkatesan R., Muthu S.E., Hatshan M.R., Vetcher A.A., Kim S.-C., Kim I. Effect of different etching times on the structural, morphological, electrical, and antimicrobial properties of mesoporous silicon // Heliyon. – 2023. – Vol. 9, No. 12. – Art. e23105. https://doi.org/10.1016/j.heliyon.2023.e23105

28. Muhammad W., Song J., Kim S., Ahmed F., Cho E., Lee H., et al. Silicon-based biosensors: A critical review of silicon's role in enhancing biosensing performance // Biosensors. – 2025. – Vol. 15. – Art. 119. https://doi.org/10.3390/bios15020119

29. Yang J.J., Grollier J., Williams R.S., Huang R. Neuromorphic engineering: From materials to device application // Advanced Materials. – 2023. – Vol. 35, No. 37. -Art. 2305078. ahttps://doi.org/10.1002/adma.202305078

30. Yakovtseva V., Volchek S., Bondarenko V., Sayyed M.I., Hanafy T.A., Trukhanov S., Bondaruk A., et al. Effects during the cathode polarization of porous silicon // Heliyon. – 2024. – Vol. 10, No. 15. – Art. e34675. https://doi.org/10.1016/j.heliyon.2024.e34675

31. Anwar S., Muhammad, Ha S.J.-H., Lee J., Song I.-H., Kim Y.-W. Controlling the electrical resistivity of porous silicon carbide ceramics and their applications: A review // International Journal of Applied Ceramic Technology. – 2022. – Vol. 19, No. 4. – Pp. 1814–1840. https://doi.org/10.1111/ijac.14034

32. Friedrich S., Stojecevic S., Rapp P., Helmer S., Bock M., Durdel A., Gasteiger H.A., Jossen A. Effect of mechanical pressure on lifetime, expansion, and porosity of silicon-dominant anodes in laboratory lithium-ion cells // Journal of the Electrochemical Society. – 2024. – Vol. 171, No. 5. – Art. 050540. https://doi.org/10.1149/1945-7111/ad36e6

Information about author:

Faten Alfeel – Assistant Professor at the Medical Physics Department, College of Science, Al-Farahidi University (Baghdad, Iraq, e-mail: faten.hussein@uoalfarahidi.edu.iq).